Fishbone structures for thermochemical energy storage in porous systems

Alexandre Malley-Ernewein, Sylvie Lorente

Fishbone structures for Thermochemical Energy Storage in porous systems

Alexandre Malley-Ernewein[1], Sylvie Lorente[1,2*]
[1]LMDC, Université de Toulouse, UPS, INSA, Toulouse, France
[2]Villanova University, Department of Mechanical Engineering, Villanova, PA 19085, USA

Abstract

This paper documents the design of a flow configuration for Thermochemical Energy Storage in a porous medium impregnated with salt. The heat transfer fluid blown through the system is humid air, and the reaction of water vapor with the salt leads to heat storage or release. A thermodynamic analysis reveals the relationship between the pore geometry and the main parameters describing the transfers (mass flow rate, reaction enthalpy and temperature difference). Relying on this result, a Fishbone architecture is proposed allowing the fluid to meander between salt inserts. It is shown that such a configuration brings compacteness to the design without loss of heat transfer and mass exchange performances. Next, an equivalent porous medium approach is used to scale up to a module made of Fishbones assemblies in alternating with heat transfer fluid channels. For constant porosity and apparent volume of the module, we show in accord with the constructal approach that an arrangement of the Fishbones for high energy efficiency exists.

Keywords: thermochemical energy storage; constructal; porous reactor

* Corresponding author: sylvie.lorente@villanova.edu

Nomenclature

Symbols

a	reaction advancement
c	water vapor molar concentration, mol/m^3
c_p	heat capacity, J/(kg K)
C	swelling coefficient
d	thickness, m
Dec	salt bed energy density, kWh/m^3
D_h	hydraulic diameter, m
D_v	water vapor diffusion coefficient, m^2/s
e	salt thickness, m
G	mass advective term, $mol/(m^3\ s)$
Δh	molar enthalpy of reaction, J/mol
H	element height, m
H_{module}	module height, m
I	heat advective term, $W/(m^3\ s)$
J	heat sink or source term, $W/(m^3\ s)$
k	thermal conductivity, W/(m K)
k_{cin}	kinetic coefficient, 1/s

K	permeability, m^2
L	channel length, m
L_0	element length, m
L_1	insert length, m
$\dot{m}$	mass flow rate, kg/s
M	molar mass, kg/mol
n_s	bulk molar density, mol/m^3
n	number of elemental Fishbones in one bed
N	number of beds in one storage module
O	mass sink or source term, $mol/(m^3\,s)$
p	pressure, Pa
p_v	partial water vapor pressure, Pa
q	heat released during the salt hydration, W
R	gas constant, J/(mol K)
Re	Reynolds number
$\dot{S}_{gen}$	entropy, J/K
T	temperature, K
t	time, s
$\mathbf{u}$	velocity vector, m/s

$\mathcal{V}$	volume, m^3
V	displacement velocity, m/s
W	element width, m
x	length, m

Greek symbols

β	efficiency coefficient
γ	reaction stochiometric coefficient
ε	salt porosity
μ	dynamic viscosity, Pa s
ν	kinematic viscosity, m^2/s
ρ	density, kg/m^3
ϕ	storage module porosity

Subscripts

eq	equilibrium
equ	equivalent
f	fluid

in	inlet
init	initial
out	outlet
s	salt
v	vapor

Subscripts

~	non dimensionnal

1. Introduction

A major challenge of our modern societies is to limit climate change. To this sake, the European Union has adopted the European Green Deal in 2019 [1] aiming to reinforce the previous objectives taken in 2009 and updated during the 2010s [2]. To reduce the greenhouse gas emissions, it is crucial to decrease the carbonated fossil energy and to increase the renewable energy share in the energy mix, while improving the efficiency of the energy systems. One of the main issues encountered with renewable energy, whether wind or solar, is the intermittency of its production and consumption, calling for solutions to store energy, long term or short term [3–6]. Among the various energy storage solutions that exist, Thermochemical Energy Storage (TES) is a promising one because it allows to prevent heat leakages and reaches high values of stored energy: the energy density of the reactive material goes from 50 to 380 kWh/m^3 and the one of the prototype ranges from 30 to 200 kWh/m^3 [7]. The need for compactness in the storage unit is one the challenges

faced by TES. The principle of storing energy thermochemically [8–10] lies in a reversible chemical reaction between two reactants − a solid and a fluid (often a gas). In this study the reactive material is a salt which characteristics correspond to strontium bromide ($SrBr_2$) and the fluid is a gas (water vapor) carried by an air flow at atmospheric pressure in an open system. This pair of reactants was selected as an example of well studied process [11–14]. When cool humid air comes in contact with the salt, the reaction between water vapor and the salt generates heat so that the exiting air is drier and warmer. On the opposite, during the storing processs, the release of water vapor molecules by the salt requires heat which is taking out of the heat transfer fluid, leading to air exiting the reactor at a higher moisture level and lower temperature than at the entrance.

When it comes to enhancing the thermochemical reactor performance, we note that most studies concern the scale of the heat exchanger or of the whole reactor [15,16]. We focus in this work on the pore scale, when a porous matrix is impregnated with salt. From a practical point of view, such strategy becomes possible to implement because, today, techniques such as robotcasting allow to 3D print with large possibilities of controlled geometry [17,18]. The analysis developped in this work relies on the constructal law [19]. The view that morphing flow configurations with purpose enhances the efficiency of any flow system is the centerpiece of the constructal approach. Applications span multiple domains [20–24], mainly in thermal science [25–28], including energy storage (sensible, latent [29,30] and TES [31,32]).

2. Thermodynamic analysis

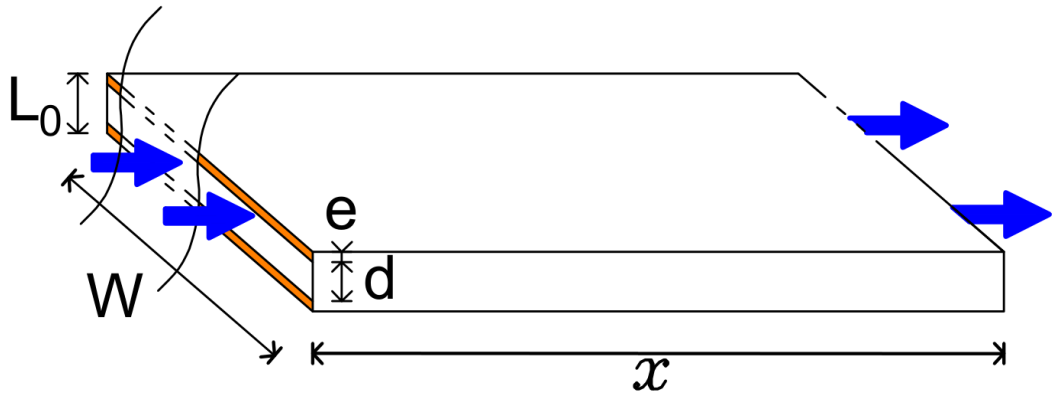

Figure 1: Rectangular pore channel impregnated with salt – not to scale

Consider a channel of length x and rectangular cross section $d \times W$. A volume of salt $\mathcal{V}_s$ is deposited uniformly along the walls. The salt thickness is e. Assume next that W is much bigger than the two other dimensions, so that the problem can be considered two-dimensional, and the hydraulic diameter is $D_h = 2d$. The volume of salt impregnating the two $d \times x$ walls is significantly smaller than the salt volume along the two $W \times x$ walls.

While the heat transfer fluid (humid air) is blown along the channel at a mass flow rate $\dot{m}$, its water vapor content reacts with the salt thanks to molecular diffusion. Insights on the tube length can be estimated from the determination of the entropy generated during the process. The heat transfer irreversibilities are given by [33]

$$\dot{S}_{gen,\Delta T} \sim \frac{q\Delta T}{T^2} \tag{1}$$

where q is the heat released during the salt hydration, $q \sim k_{cin} \Delta h \, n_s \mathcal{V}_s$. Here ΔT is the temperature change experienced by the fluid during the salt hydration, k_{cin} is the kinetic constant of the salt

reaction, Δh is the enthalpy released during hydration, and n_s is the molar density of the reactive salt.

Assuming an ideal gas, the fluid friction irreversibilities are given by

$$\dot{S}_{gen,\Delta p} \sim \dot{m} R_v \ln \frac{p_{in}}{p_{out}} \tag{2}$$

where R_v is the ratio of R the gas constant and M_v the vapor molar mass. As the pressure difference along the pipe, Δp, is much smaller than the atmospheric pressure, $ln \frac{p_{in}}{p_{out}} \cong \frac{\Delta p}{p_{in}}$ [34]. Therefore

$$\dot{S}_{gen,\Delta p} \sim \frac{12\nu}{W d^3} \frac{\dot{m}^2 x}{\rho_f T} \tag{3}$$

Because, in laminar flow, Δp scales as $12\ \nu\ \dot{m}\ x/Wd^3$.

The balance between heat transfer and fluid irreversibilities leads to

$$x \sim \frac{n_s \mathcal{V}_s k_{cin} \Delta h}{12\nu \dot{m}^2} \rho_f W d^3 \frac{\Delta T}{T} \tag{4}$$

Equation 4 shows that when the boundary conditions are fixed (mass flow rate and inlet temperature) and the salt characteristics and salt amount are also fixed, the elemental channel length dictates the temperature increase of the heat transfer fluid that leaves the channel. Because space is constrained, improving the performance of the element means to change its configuration towards more compactness in the space occupied by the surface of exchange between the heat transfer fluid and the salt, while acknowledging a penalty in terms of friction losses.

3. Modelling

The numerical analysis consists in solving the mass, momentum and energy conservation equations, considering laminar flow within the fluid channel, and molecular diffusion through the salt.

The heat transfer fluid is humid air. Water vapor is the active component that triggers the thermochemical reaction while diffusing within the salt. Therefore, in addition to the mass conservation of humid air within the channel (Eq. (5)), the conservation of the mass of water vapor must be written within the channel and the salt (Eq. (6)). Equation (7) gives the momentum equation. The first law of thermodynamics is written for the entire system (channel and salt, Eq. (8)). Finally, Eqs. (9) and (10) give respectively the rate of the reaction advancement for the salt hydration and for the salt dehydration.

$$\frac{\mathrm{D}\rho_\mathrm{f}}{\mathrm{D}t} = 0 \tag{5}$$

where ρ_f is the density of humid air. It is assumed that the changes in water vapor content do not impact the humid air properties [14].

$$\frac{\mathrm{D}\mathbf{u}}{\mathrm{D}t} = -\frac{1}{\rho_\mathrm{f}}\boldsymbol{\nabla}\mathrm{p} + \nu\boldsymbol{\nabla}^2\mathbf{u} \tag{6}$$

where $\boldsymbol{u}$ is the humid air velocity vector, ν is the kinematic viscosity.

$$\frac{\partial \mathrm{c}}{\partial t} + \boldsymbol{\nabla}\left(-\mathrm{D}_{\mathrm{v,i}}\boldsymbol{\nabla}\mathrm{c}\right) + \mathrm{G}_\mathrm{i} = \mathrm{O}_\mathrm{i} \tag{7}$$

where c is the water vapor concentration. The subscript i is either s the salt or f for the fluid (humid air). $D_{v,s}$ and $D_{v,f}$ are the diffusions coefficient of water vapor in the salt and in the fluid

respectively. We have: $G_f = (\boldsymbol{u} \cdot \boldsymbol{\nabla})c$, $G_s = 0$, $O_f = 0$, $O_s = -\gamma\, n_s \frac{\partial a}{\partial t}$, where γ is the stochiometric coefficient of the reaction and a is the reaction advancement.

$$\rho_i\, c_{p_i} \frac{\partial T}{\partial t} + \boldsymbol{\nabla} \cdot (k_i\, \boldsymbol{\nabla} T) + I_i = J_i \tag{8}$$

where c_{p_s} and c_{p_f} are the salt and fluid heat capacity respectively, k_s and k_f are the salt and the fluid thermal conductivity respectively. $I_f = \left(\rho_f\, c_{p_f}\, \boldsymbol{u} \cdot \boldsymbol{\nabla}\right) T$, $I_s = 0$, $J_f = 0$, $J_s = n_s \frac{\partial a}{\partial t} \Delta h$.

$$\frac{\partial a}{\partial t} = k_{cin} \left(1 - \frac{p_{eq}}{p_v}\right)(1 - a) \tag{9}$$

$$\frac{\partial a}{\partial t} = k_{cin} \left(1 - \frac{p_{eq}}{p_v}\right) a \tag{10}$$

where p_{eq} is the equilibrium pressure, and p_v is the vapor partial pressure.

The initial and boundary conditions are identical to the ones described in Ref. [35]: the initial temperature is T_{init}, and the initial vapor concentration is c_{init}. This concentration corresponds to the equilibrium vapor pressure at temperature T_{init}. The fluid is initially motionless at atmospheric pressure. Table 1 to 3 give the set of data used in the simulations. The salt characteristics are the ones of the $SrBr_2$ [14].

The mass flow rate ṁ, water vapor concentration, c_{in}, and the temperature, T_{in}, are constant at the channel entrance. The mass flow rate value ensures to remain in the laminar region. The entrance length is chosen greater than $0.05\, Re_{D_h} \times d$ [36] to allow a fully developed flow. The outlet boundary conditions are atmospheric pressure and thermal outflow. The external walls of the channels are thermally insulated with no vapor flux. A no-slip condition is imposed at the fluid/salt interface.

When molecules of water vapor react with the salt, an increase in volume of the now hydrated salt may be expected, depending on the dimensions and geometry. Assuming the impregnated salt layer is pure salt, the swelling is directed perpendicularly to the wall, in the fluid channel. Numerically, swelling leads to the modelling of moving boundaries and interfaces. To account for this, we added a displacement velocity $\boldsymbol{V}$ perpendicular to each salt interface, directed from the salt toward the fluid channel. This velocity is proportional to the reaction advancement rate (Eq. (11)).

$$\mathbf{V} = \mathrm{C}\frac{\partial \mathrm{a}}{\partial \mathrm{t}} \tag{11}$$

where *C* is a swelling coefficient obtained from the experimental data of Ref. [14].

In [14], ε the porosity of the reactive material, which is arranged in beds, evolves during the salt reaction: the porosity value goes from 0.684 when the salt bed is fully dehydrated (FD) to 0.383 when it is fully hydrated (FH). The porosity is calculated with the salt bed energy density *Dec*, the enthalpy of reaction Δh, the salt density ρ_s and the salt molar mass M_s). Knowing that $\varepsilon = (1- \mathcal{V}_s) / \mathcal{V}_{app}$ and $\mathcal{V}_{app}$ is constant, we calculate $\mathcal{V}_{s,FH} / \mathcal{V}_{s,FD} = 1.95$. Because the velocity is defined at the salt/fluid boundary, the swelling coefficient *C* is equal to $e \times (1.95\text{-}1)$.

The set of equations is solved with a FEM code [37]. The verification and validation of the numerical approach were presented in earlier works [35,38,39] and are not repeated here. The mesh chosen for the study consists of 530,000 elements, with refinements located at the boundaries between the fluid domain and the salt domain, and within the salt domain. The test on the mesh accuracy was based on mass and energy conservation at the scale of the entire element. With 530,000 elements, mass and energy conservation was ensured with a 2% margin of error which was considered accurated enough.

Table 1: Initial and boundary conditions, adapted from [14,35,40,41].

Parameter (unit)	Value
c_{in} (mol/m^3)	0.406
c_{init} (mol/m^3)	0.056
$\dot{m}_{in}$ (kg/s)	4.98 10^{-10}
$p_{v,in}$ (Pa)	997
$p_{v,init}$ (Pa)	137
T_{in} (°C)	25
T_{init} (°C)	20

Table 2: Fluid properties, adapted from [14,35,40,41].

Fluid property	Value
μ (Pa.s)	1.830 10^{-5}
ρ_f (kg/m^3)	1.179
c_{p_f} (J/(kg.K))	1011.9
$D_{v,f}$ (m^2/s)	2.6 10^{-5}
k_f (W/(m.K))	0.026

Table 3: Properties of the reacting salt SrB_2, adapted from *[14,35,40,41]*.

SrB_2 property	Value
Δh (J/mol)	3.37 10^5

$\rho_s = \rho_{FD} + a(\rho_{FH} - \rho_{FD})$ (kg/m^3)	$\rho_{FD} = 3481$ $\rho_{FH} = 2390$
$c_{p_s} = c_{p_{s,FD}} + a\left(c_{p_{s,FH}} - c_{p_{s,FD}}\right)$ (J/(kg.K))	$c_{p_{s,FD}} = 456$ $c_{p_{s,FH}} = 968$
$D_{v,s}$ (m^2/s)	$1.2\ 10^{-13}$
k_{cin} (1/s)	$8\ 10^{-6}$
k_s (W/(m.K))	1
$M_s = M_{s,FD} + a(M_{s,FH} - M_{s,FD})$ (kg/mol)	$M_{s,FD} = 0.26544$ $M_{s,FH} = 0.35552$
n_s (mol/m^3) (calculated from [14] for a pure salt layer)	13144
FD = fully dehydrated, FH = fully hydrated	

The impact of swelling on the reaction advancement was tested in the case of a straight channel of rectangular cross section $d \times W = 10\ \mu m \times 1\ m$. To simulate salt impregnation, the interior of the walls was covered by a salt layer of thickness *e*. The tested values were *e* = 0.5, 1, 2 and 2.5 µm. The simulations were run in two cases: with and without swelling. As shown in Figure 2, swelling does not have effect on the results up to a salt thickness *e* = 1 µm. Beyond this value the figure shows that swelling leads to an increase in the time needed for the complete advancement of the reaction. For example, the time to obtain the total hydration of the salt is multiplied by 2 when the thickness of the dehydrated salt is 2.5 µm. In the rest of the paper, the salt thickness was kept at *e* = 1 µm.

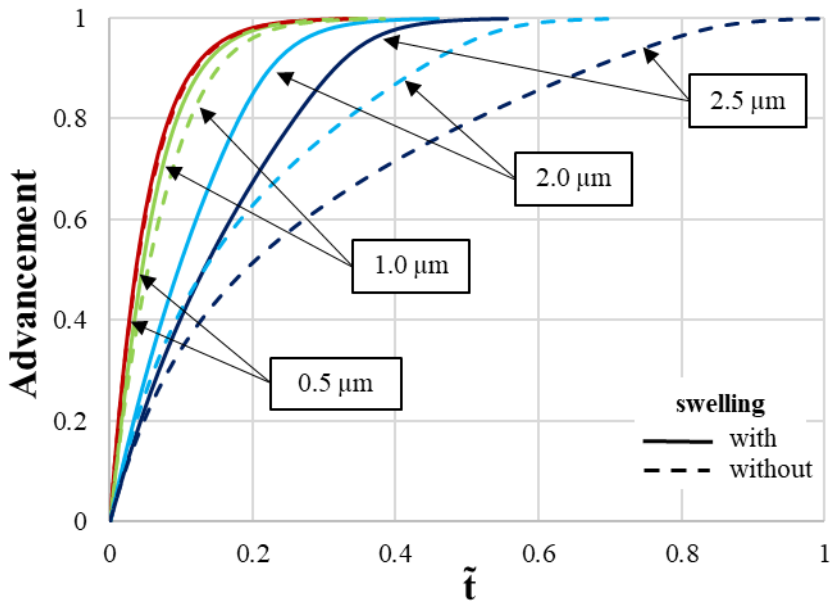

Figure 2: Reaction advancement in a straight channel with various salt layer thicknesses as a function of the dimensionless time, with and without swelling.

4. The Fishbone element

In the search for an increase in compactness, the channel geometry was changed to maintain the flow path to the value obtained in Eq. (4) while reducing the footprint of the element. In the new channels, the heat transfer fluid meanders between salt inserts. The assembly of channels in parallel leads to a structure of the salt inserts resembling a Fishbone. The resulting Fishbone salt configuration is shown in Fig. 3. Note that such change allows to meet the requirement of constant elemental fluid and salt volumes.

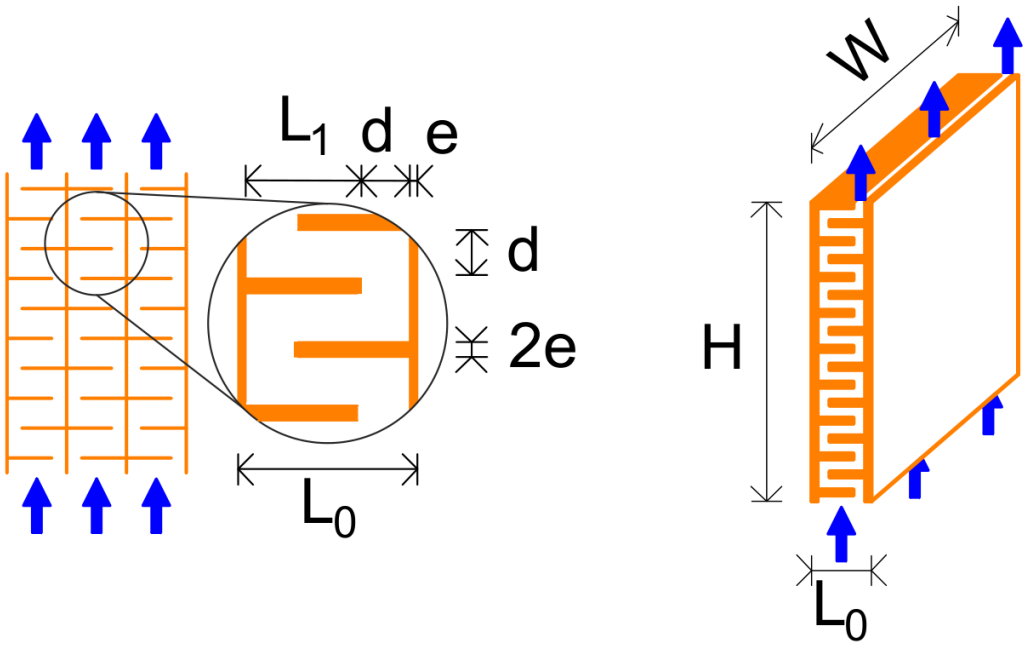

Figure 3: Fishbone structure (left) and zoom on an elemental pattern (right) – not to scale.

The Fishbone architecture consists in folding the rectilinear channel into an elemental system of height H, width W, and length L_0. The fluid cross section remains $d \times W$. The length of each insert, or "bone of the fish", L_1, is calculated from the salt volume which is maintained at the same value as in the rectilinear channel. Hence, $L_0 = L_1 + d + 2e$. The generated pattern is regularly repeated within the elemental system. For example, the case that is numerically tested in the next section is made of 416 patterns fitting within H = 1 cm, the height of the element. Folding the rectilinear channel into the Fishbone configuration does not impact the overall pressure change because for such low Reynolds number the inertia term into the momentum conservation equation becomes negligible compared to friction (creeping flow). This was demonstrated by modeling only the fluid mechanics part of the problem and comparing the pressure change between inlet and outlet in the case of the Fishbone and in the case of the rectilinear channel with identical fluid volume (see Table 4).

Table 4: Geometrical dimensions, and pressure drop (Fishbone and straight channel).

Type	H (cm)	L_0 (µm)	W (m)	Flowpath (cm)	V_{fluid} (m^3)	V_{salt} (m^3)	Q_{in} (m^3/s)	Δp (Pa)
Fishbone	1	80	1	6.7	6.66×10^{-7}	1.33×10^{-7}	2.5×10^{-7}	3.4×10^{3}
straight channel	6.7	12	1	6.7	6.66×10^{-7}	1.33×10^{-7}	2.5×10^{-7}	3.4×10^{3}

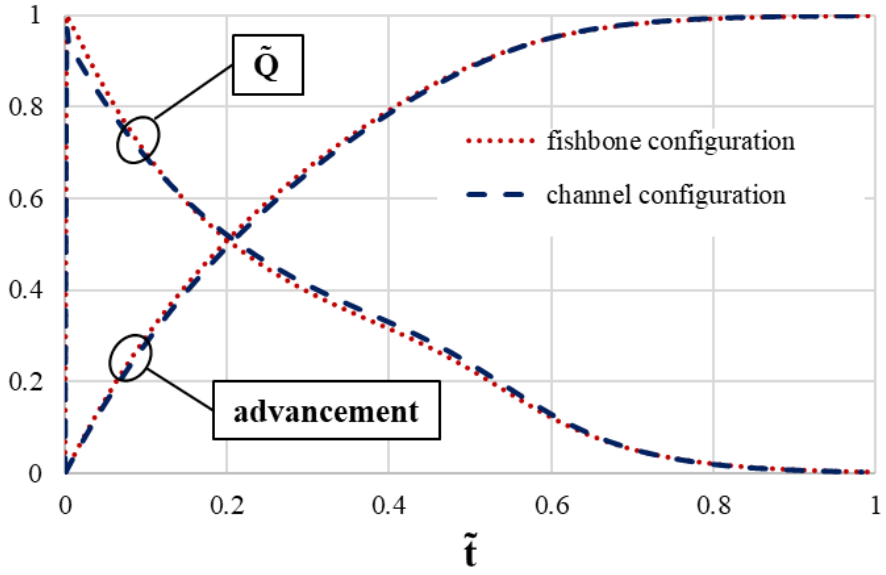

Figure 4: Reaction advancement and non-dimensional heat released as a function of the non-dimensional time for a straight channel and for the Fishbone configuration.

Figure 4 presents the reaction advancement and the amount of heat released in time. The latter is given in a non-dimensional way by dividing each value by the maximum value obtained in the fully hydrated Fisbone configuration. The reaction advancement remains the same in both cases, rectilinear channel and Fishbone channel, with a steep slope at the start of the salt hydration that decreases in time when less and less molecules of salt are available to react with the molecules of

water vapor. Zooming at *H/2*, we show in Fig. 5 the water vapor concentration map within the Fishbone element at various hydration times, together with the velocity vector. Note that the humid air is meandering along the channel while the salt becomes hydrated in time. The salt hydration is depicted in the figure by the increase in water concentration. Hydration starts at the tip of the salt inserts before spreading throughout the entire volume of salt.

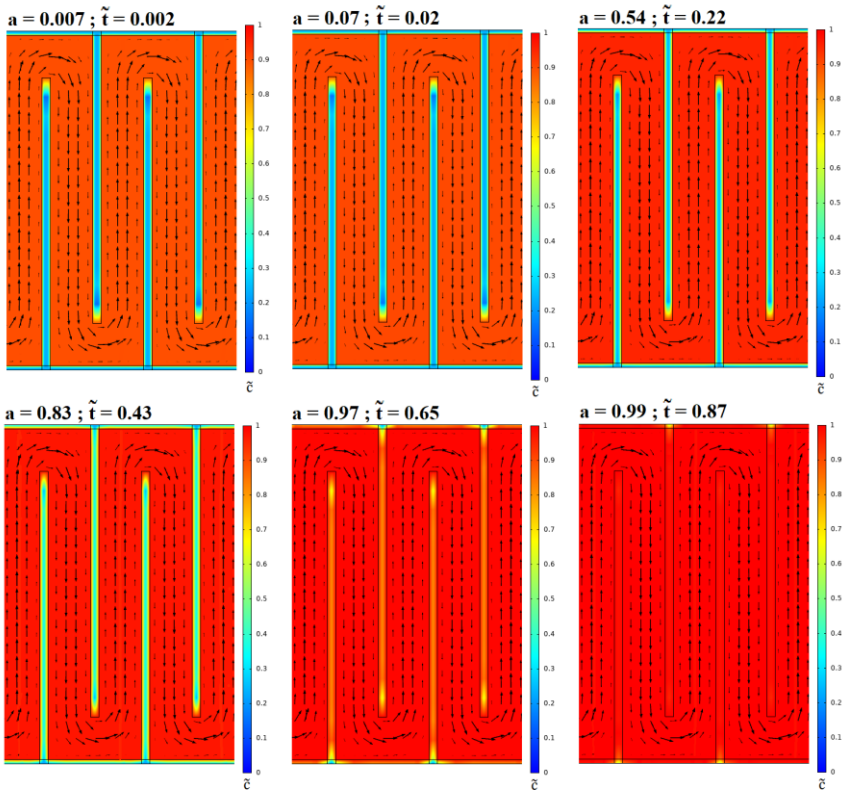

Figure 5: Non-dimensional water vapor concentration ($\tilde{c} = c\,/c_{in}$) and velocity at different reaction advancements at mid-distance within the Fishbone.

5. Upscaling to a salt bed

Consider now a reactor module made of an assembly of salt beds in parallel as shown in Fig. 6. The typical dimensions of each side are about 10 cm (see Ref. [38] for more details). The salt beds alternate with inlet channels and outlet channels, in such a way that the heat transfer fluid entering

the channels is forced to flow through its neighboring salt layer as the inlet channel exit is closed. By the same token, the fluid is driven towards the outside of the module once it has crossed the salt beds.

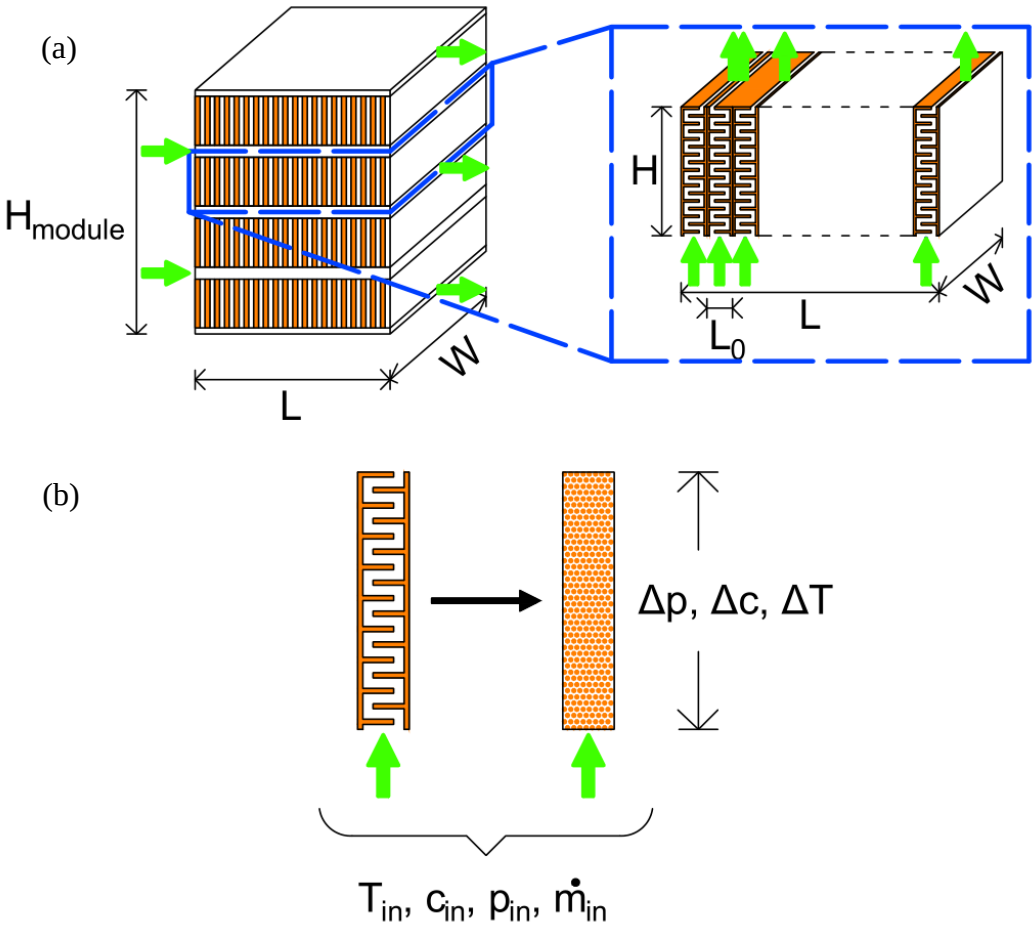

Figure 6: (a) Module made of the assembly of salt beds and air channels, with the details of a salt bed made of Fishbone elements in parallel, and (b) equivalent porous-media approach to describe heat, fluid and mass transport through the Fishbone element.

Assuming that each salt layer consists in identical Fishbone structures placed in parallel (see Fig. 6), about n = 1250 elemental Fishbones would be necessary for one single salt bed of L = 10 cm. The corresponding computational power needed for the numerical simulations at the salt bed scale would be so massive that another approach was preferred. Without loss of accuracy,

we determined the properties of a porous material equivalent to the Fishbone element. The volume of salt and the volume of the air passages were used to calculate the porosity $\varepsilon_{\mathrm{equi}}$ of the equivalent porous element. The pressure difference between the inlet of the Fishbone and its outlet was extracted from the numerical results obtained in Section 4. An equivalent permeability was then calculated for an approach of the fluid flow through the bed based on Darcy's law (Eq. 12).

Table *5* gives the properties of the equivalent porous material obtained with this approach. Note that the term representing the sink or source of water vapor in Eq. (7) was corrected by a factor of 2.1 in order to match the results of the model based on the complete resolution of the set of Equations (5) to (10).

$$K = \frac{\mu\, \dot{m}_{in}}{\rho(L_0 - 2e)W} \frac{H}{\Delta p} \qquad (12)$$

Figure 7 gives the reaction advancement as a function of the non-dimensional time (Fig. 7a), together with the non-dimensional heat released (Fig. 7b), the non-dimensional pressure change (Fig. 7c) and the non dimensional vapor concentration change (Fig. 7d) for the Fishbone and for its equivalent porous medium. The porous medium approach provides results similar to the ones obtained when modeling the heat and mass exchanges in the Fishbone with the set of equations proposed in Section 3, and was therefore kept for the simulation of the entire module.

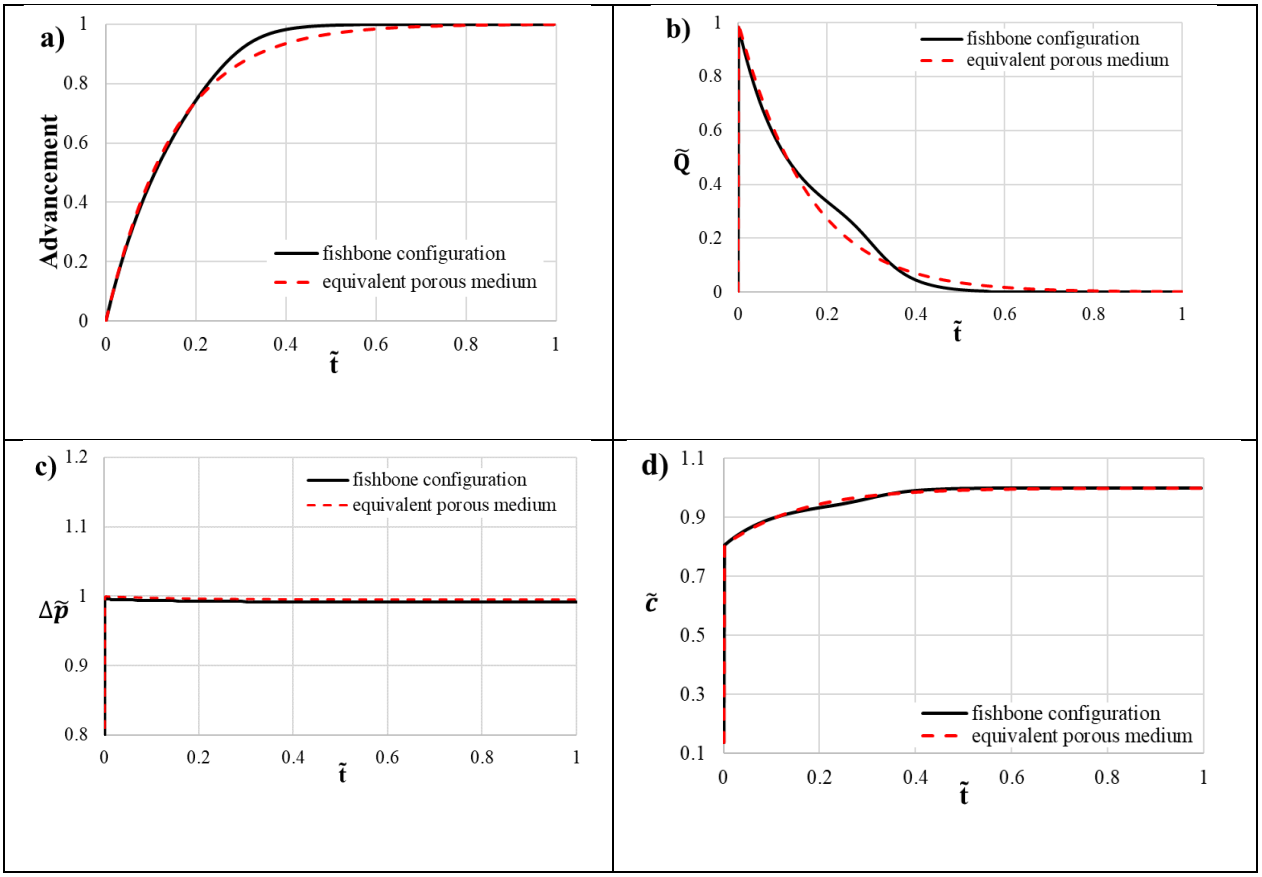

Figure 7: Comparison between the thermodynamics properties (reaction advancement, heat released, pressure losses and outlet vapor concentration) of the Fishbone model (solid lines) and the equivalent porous medium approach (dotted lines) as a function of the non-dimensional time.

Table 5: Equivalent porous medium characteristics (the salt characteristics are in Table 3).

Equivalent porous medium characteristic	**Value**
$\rho_{equ} = \varepsilon_{equ}\rho_f + (1-\varepsilon_{equ})\rho_s$ (kg/m^3)	
$Cp_{equ} = \varepsilon_{equ}Cp_f + (1-\varepsilon_{equ})Cp_s$ (J/kg/K)	
ε_{equ}	0.833
k_{equ} (W/(m.K))	0.24
$n_{s,equ}$ (mol/m^3) (average value weighted by the relative volume of fluid and salt)	2185.7
K (m^2)	1.61 10^{-13}

$k_{cin,equ}$ (1/s)	$3\ 10^{-6}$
note: $k_{cin,equ}$ was determined through numerical simulations by fitting the Fishbone and equivalent porous medium results	

Assume next that the apparent volume of the module $\mathcal{V} = H_{module} \times L \times W$ is fixed, together with the volume of salt. The apparent porosity ϕ is given by the ratio of the air channels between salt layers and the apparent volume of the module. This means that in this definition we do not account for the Fishbone intrinsic porosity (or its porous medium counterpart), which is also a constant as mentioned previously. We fix $\phi = 0.8$. The question is how to distribute the salt beds within the entire volume so that the system performs at best: should the salt beds by constituted of few large elements or many small ones? To answer this question, we invoke one of the feature of the constructal law: the equipartition of thermodynamic imperfections, as in [37]. The number of parallel salt layers can be obtained by balancing the pressure losses along the heat transfer fluid channels and the pressure changes through each salt bed. Following the methodology developed in Ref. [37], and not repeated here, we obtain:

$$12\ \mathrm{K} \sim \frac{\phi^3(1-\phi)\mathrm{H}_{\mathrm{module}}^4 \mathcal{V}^2}{\mathrm{N}^2\mathrm{L}^2\left[\left(\phi\mathrm{L}\mathrm{H}_{\mathrm{module}}^2\right)^2 + (\mathrm{N}\mathcal{V})^2\right]} \tag{13}$$

where H_{module}, L and $\mathcal{V}$ are the module height, length and apparent volume respectively. N is the total number of beds in the module and K is the Fishbones bed permeability defined for the equivalent porous medium.

As shown in Fig. 8, equipartition is obtained when the number of salt layers is about 70 when $K = 1.61\ 10^{-13}$ m^2, $H_{module} = L = W = 10$ cm and $\phi = 0.8$.

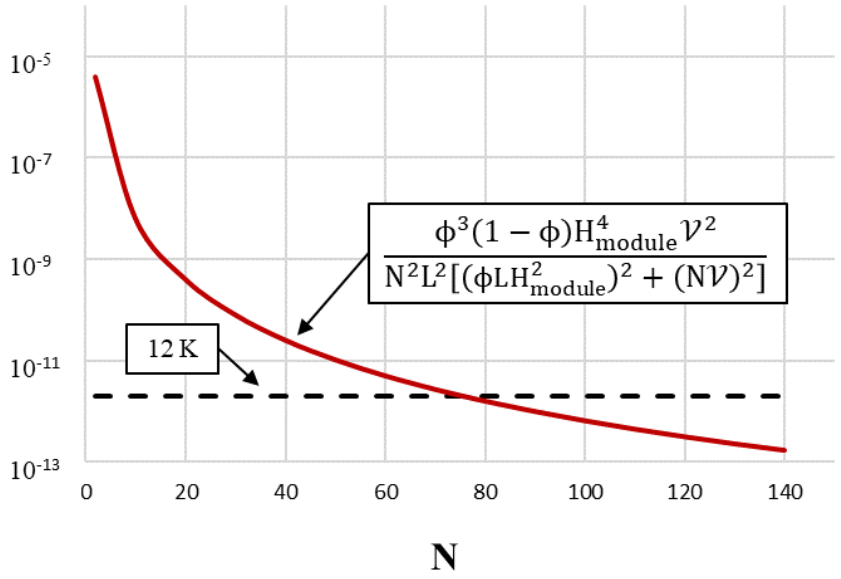

Figure 8: The two terms of Eq. 13 as a function of the number of salt layers *N*.

To confirm this result, a series of numerical simulations was run in the case of a cubic module of side 10 cm containing 10, 50, 80 and 100 salt layers with an overall blown mass flow rate of 2.92 10^{-1}g/s and the boundary conditions in temperature, vapor concentration and pressure listed in Table 1. The mass flow rate comes from experimental works [7] and was taken proportional to the salt volume. This value was used in a previous study [38] as the mass flow rate blown in one storage module. Recall that each salt layer is the porous medium equivalent to 1250 Fishbones in parallel. The results are summarized in Fig. 9 for different values of the reaction advancement. Plotted on the ordinate is β the energy performance given by the ratio of heat released by the chemical reaction and the pumping power necessary to blow the heat transfer fluid through the entire module. The results indicate that separating the salt volume into about 55 parallel salt layers produces a higher β coefficient. This value is within the order of magnitude of the prediction from Eq. (13).

Finally, a parametric study was performed to determine the shape factor of the module leading to the best energy performance, while the overall module volume, porosity and height remained constant. The energy performance ratio reaches its maximum at the very beginning of the reaction advancement which corresponds to the highest heat released while the pumping power remains constant. The ratio then decreases in time as the reaction advancement progresses. Figure 8 shows the evolution of the energy performance ratio when changing the shape of the module. Clearly, shorter and therefore wider air channels separating the salt layers allow to increase the energy performance of the entire module.

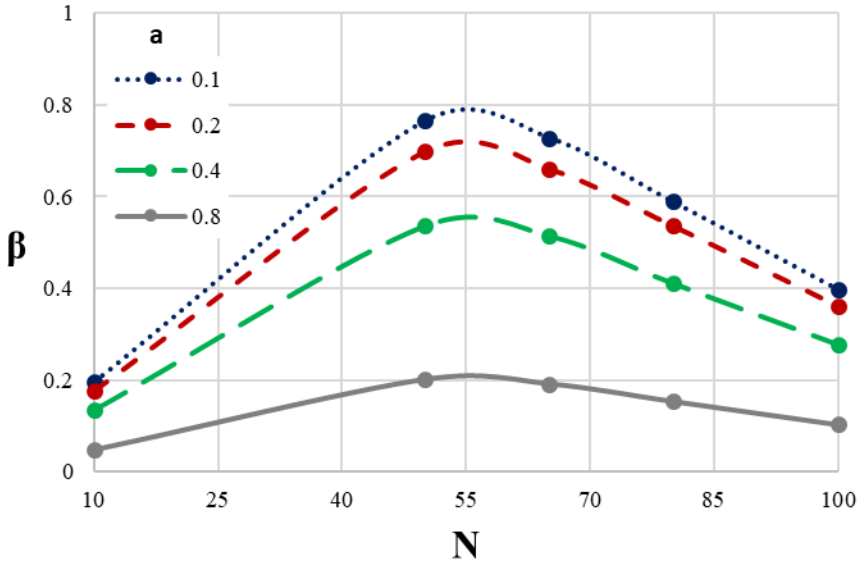

Figure 9: Energy ratio β at different advancements as a function of the number of salt layers N for constant module dimensions.

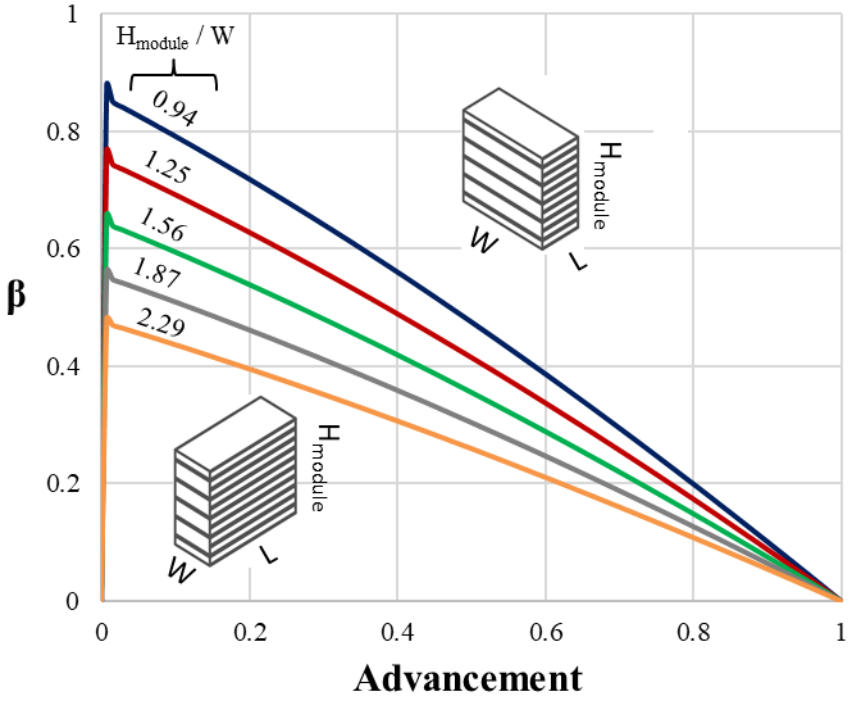

Figure 10: Energy ratio β as a function of the reaction advancement for different module dimensions.

Conclusion

The objective of this work was to uncover a new kind of salt architecture for Thermochemical Energy Storage within a porous system. It is shown from thermodynamic analysis balancing heat transfer and fluid friction irreversibilities that a relationship between the geometrical features of the pore channels and the thermodynamic characteristics exists. The search for compactness in the configuration leads to Fishbone architectures in which the heat tranfer fluid is allowed to meander between salt inserts. By folding channels into Fishbone architectures at constant salt volume and heat transfer fluid volume, it was demonstrated that the resulting module made of layers of assemblies of Fishbones can be morphed into a highly compact ensemble with high energy efficiency.

References

[1] European Commission, COMMUNICATION FROM THE COMMISSION The European Green Deal, (2019). https://eur-lex.europa.eu/legal-content/EN/TXT/HTML/?uri=CELEX:52019DC0640&from=EN (accessed June 7, 2021).

[2] European Union, DIRECTIVE 2009/28/EC OF THE EUROPEAN PARLIAMENT AND OF THE COUNCIL of 23 April 2009 on the promotion of the use of energy from renewable sources and amending and subsequently repealing Directives 2001/77/EC and 2003/30/EC, (2009). https://eur-lex.europa.eu/legal-content/EN/TXT/PDF/?uri=CELEX:32009L0028.

[3] A. Gautam, R.P. Saini, A review on technical, applications and economic aspect of packed bed solar thermal energy storage system, J. Energy Storage. 27 (2020) 101046. https://doi.org/10.1016/j.est.2019.101046.

[4] A. Gautam, R.P. Saini, Performance analysis and system parameters optimization of a packed bed solar thermal energy storage having spherical packing elements with pores, J. Energy Storage. 48 (2022) 103993. https://doi.org/10.1016/j.est.2022.103993.

[5] A. Sharma, R. Pitchumani, R. Chauhan, Solar air heating systems with latent heat storage - A review of state-of-the-art, J. Energy Storage. 48 (2022) 104013. https://doi.org/10.1016/j.est.2022.104013.

[6] F. Ma, L. Liu, L. Ma, Q. Zhang, J. Li, M. Jing, W. Tan, Enhanced thermal energy storage performance of hydrous salt phase change material via defective graphene, J. Energy Storage. 48 (2022) 104064. https://doi.org/10.1016/j.est.2022.104064.

[7] B. Michel, N. Mazet, P. Neveu, Experimental investigation of an innovative thermochemical process operating with a hydrate salt and moist air for thermal storage of solar energy: Global performance, Appl. Energy. 129 (2014) 177–186. https://doi.org/10.1016/j.apenergy.2014.04.073.

[8] R. Fisher, Y. Ding, A. Sciacovelli, Hydration kinetics of K2CO3, MgCl2 and vermiculite-based composites in view of low-temperature thermochemical energy storage, J. Energy Storage. 38 (2021) 102561. https://doi.org/10.1016/j.est.2021.102561.

[9] R.-J. Clark, M. Farid, Experimental investigation into the performance of novel SrCl2-based composite material for thermochemical energy storage, J. Energy Storage. 36 (2021) 102390. https://doi.org/10.1016/j.est.2021.102390.

[10] B. Mette, H. Kerskes, H. Drück, Concepts of long-term thermochemical energy storage for solar thermal applications – Selected examples, Energy Procedia. 30 (2012) 321–330. https://doi.org/10.1016/j.egypro.2012.11.038.

[11] K.E. N'Tsoukpoe, T. Schmidt, H.U. Rammelberg, B.A. Watts, W.K.L. Ruck, A systematic multi-step screening of numerous salt hydrates for low temperature thermochemical energy storage, Appl. Energy. 124 (2014) 1–16. https://doi.org/10.1016/j.apenergy.2014.02.053.

[12] L. Farcot, N. Le Pierrès, J.-F. Fourmigué, Experimental investigation of a moving-bed heat storage thermochemical reactor with SrBr2/H2O couple, J. Energy Storage. 26 (2019) 101009. https://doi.org/10.1016/j.est.2019.101009.

[13] A. Fopah-Lele, J.G. Tamba, A review on the use of SrBr2·6H2O as a potential material for low temperature energy storage systems and building applications, Sol. Energy Mater. Sol. Cells. 164 (2017) 175–187. https://doi.org/10.1016/j.solmat.2017.02.018.

[14] B. Michel, N. Mazet, P. Neveu, Experimental investigation of an open thermochemical process operating with a hydrate salt for thermal storage of solar energy: Local reactive bed

evolution, Appl. Energy. 180 (2016) 234–244. https://doi.org/10.1016/j.apenergy.2016.07.108.
[15] K. Kant, A. Shukla, D.M.J. Smeulders, C.C.M. Rindt, Performance analysis of a K2CO3-based thermochemical energy storage system using a honeycomb structured heat exchanger, J. Energy Storage. 38 (2021) 102563. https://doi.org/10.1016/j.est.2021.102563.
[16] P. Berdiyeva, A. Karabanova, D. Blanchard, B.C. Hauback, S. Deledda, Sr(NH3)8Cl2-Expanded Natural Graphite composite for thermochemical heat storage applications studied by in-situ neutron imaging, J. Energy Storage. 34 (2021) 102176. https://doi.org/10.1016/j.est.2020.102176.
[17] L. Tabard, E. Prud'Homme, V. Garnier, L. Gremillard, Hierarchical salt-ceramic composites for efficient thermochemical energy storage, Appl. Mater. Today. 20 (2020) 100658. https://doi.org/10.1016/j.apmt.2020.100658.
[18] L. Tabard, V. Garnier, E. Prud'Homme, E.-J. Courtial, S. Meille, J. Adrien, Y. Jorand, L. Gremillard, Robocasting of highly porous ceramics scaffolds with hierarchized porosity, Addit. Manuf. 38 (2021) 101776. https://doi.org/10.1016/j.addma.2020.101776.
[19] A. Bejan, Street network theory of organization in nature, J. Adv. Transp. 30 (1996) 85–107. https://doi.org/10.1002/atr.5670300207.
[20] A. Bejan, J.H. Marden, The constructal unification of biological and geophysical design, Phys. Life Rev. 6 (2009) 85–102. https://doi.org/10.1016/j.plrev.2008.12.002.
[21] R.G. Kasimova, D. Tishin, Yu.V. Obnosov, G.M. Dlussky, F.B. Baksht, A.R. Kacimov, Ant mound as an optimal shape in constructal design: Solar irradiation and circadian brood/fungi-warming sorties, J. Theor. Biol. 355 (2014) 21–32. https://doi.org/10.1016/j.jtbi.2014.01.038.
[22] P.M. Rodrigues, C. Biserni, C.C. de Escobar, L.A.O. Rocha, L.A. Isoldi, E.D. dos Santos, Geometric optimization of a lid-driven cavity with two rectangular intrusions under mixed convection heat transfer: A numerical investigation motivated by constructal design, Int. Commun. Heat Mass Transf. 117 (2020) 104759. https://doi.org/10.1016/j.icheatmasstransfer.2020.104759.
[23] A. Bejan, Two hierarchies in science: the free flow of ideas and the academy, Int. J. Des. Nat. Ecodynamics. 4 (2010) 386–394. https://doi.org/10.2495/DNE-V4-N4-386-394.
[24] S. Lorente, M. Hautefeuille, A. Sanchez-Cedillo, The liver, a functionalized vascular structure, Sci. Rep. 10 (2020) 16194. https://doi.org/10.1038/s41598-020-73208-8.
[25] F.B. Teixeira, C. Biserni, P.V. Conde, L.A.O. Rocha, L.A. Isoldi, E.D. dos Santos, Geometrical investigation of bluff bodies array subjected to forced convective flows for different aspect ratios of frontal body, Int. J. Therm. Sci. 161 (2021) 106724. https://doi.org/10.1016/j.ijthermalsci.2020.106724.
[26] W. Tang, H. Feng, L. Chen, Z. Xie, J. Shi, Constructal design for a boiler economizer, Energy. 223 (2021) 120013. https://doi.org/10.1016/j.energy.2021.120013.
[27] E.M. Nava-Arriaga, A. Hernandez-Guerrero, J.L. Luviano-Ortiz, A. Bejan, Heat sinks with minichannels and flow distributors based on constructal law, Int. Commun. Heat Mass Transf. 125 (2021) 105122. https://doi.org/10.1016/j.icheatmasstransfer.2021.105122.
[28] A. Almerbati, Hexagonal and mixed arrays of flow channel design in counterflow heat exchanger, Int. Commun. Heat Mass Transf. 124 (2021) 105268. https://doi.org/10.1016/j.icheatmasstransfer.2021.105268.
[29] M. Eslami, M.A. Bahrami, Sensible and latent thermal energy storage with constructal fins, Int. J. Hydrog. Energy. 42 (2017) 17681–17691. https://doi.org/10.1016/j.ijhydene.2017.04.097.

[30] S. Lorente, Design of a Latent Thermal Energy Storage System From Constructal Approach, ASME 2017 Int. Mech. Eng. Congr. Expo. 8 (2017) V008T10A063. https://doi.org/10.1115/IMECE2017-70594.
[31] Y. Azoumah, N. Mazet, P. Neveu, Optimal Design of Thermochemical Reactors Based on Constructal Approach, AIChE J. 53 (2007) 1257–1266. https://doi.org/10.1002/aic.11152.
[32] S. Tescari, N. Mazet, P. Neveu, Constructal method to optimize solar thermochemical reactor design, Sol. Energy. 84 (2010) 1555–1566. https://doi.org/10.1016/j.solener.2010.06.015.
[33] A. Bejan, S. Lorente, D.-H. Kang, Constructal design of regenerators, Int. J. Energy Res. 37 (2013) 1509–1518. https://doi.org/10.1002/er.2960.
[34] A. Bejan, Advanced Engineering Thermodynamics, 4th ed., 2016. https://onlinelibrary.wiley.com/doi/book/10.1002/9781119245964.
[35] A. Malley-Ernewein, S. Lorente, Analysis of thermochemical energy storage in an elemental configuration, Sci. Rep. 9 (2019) 1–9. https://doi.org/10.1038/s41598-019-52249-8.
[36] H.L. Langhaar, Steady flow in the transition length of a straight tube, J. Appl. Mech. 9 (1942).
[37] COMSOL Multiphysics, n.d.
[38] A. Malley-Ernewein, S. Lorente, Constructal design of thermochemical energy storage, Int. J. Heat Mass Transf. 130 (2019) 1299–1306. https://doi.org/10.1016/j.ijheatmasstransfer.2018.10.097.
[39] A. Malley-Ernewein, S. Lorente, The shape of the elemental system in a porous medium designed for thermochemical energy storage, Int. J. Heat Mass Transf. 158 (2020) 119975. https://doi.org/10.1016/j.ijheatmasstransfer.2020.119975.
[40] T. Esaki, N. Kobayashi, Reaction Rate Characteristics of SrBr2 Hydration System for Chemical Heat Pump Cooling Mode, J. Mater. Sci. Chem. Eng. 04 (2016) 106. https://doi.org/10.4236/msce.2016.42012.
[41] E.L. Cussler, Diffusion, mass transfer in fluid systems, Cambridge University Press, Cambridge [Cambridgeshire] ; New York, 1984.